



**Influence of Polyethylene Glycol Passivation on the Surface Plasmon Resonance Induced Photothermal Properties of Gold Nanorods**

Journal:	<i>Nanoscale</i>
Manuscript ID	NR-ART-04-2018-003026.R1
Article Type:	Paper
Date Submitted by the Author:	25-May-2018
Complete List of Authors:	Marasini, Ramesh; Kansas State University College of Arts and Sciences, Chemistry Pitchaimani, Arunkumar; Kansas State University, Anatomy and Physiology; Nguyen, Tuyen; Kansas State University, Chemistry; Kansas State University Comer, Jeffrey; Kansas State University, Anatomy and Physiology Aryal, Santosh; Kansas State University, Chemistry



Journal Name

ARTICLE

## Influence of Polyethylene Glycol Passivation on the Surface Plasmon Resonance Induced Photothermal Properties of Gold Nanorods

Received 00th January 20xx,  
Accepted 00th January 20xx

DOI: 10.1039/x0xx00000x

www.rsc.org/

Ramesh Marasini<sup>a, b</sup>, Arunkumar Pitchaimani<sup>b</sup>, Tuyen Duong Thanh Nguyen<sup>a, b</sup>, Jefferey Comer<sup>b</sup>, Santosh Aryal<sup>\*a, b</sup>

Gold nanorods (AuNRs) possess unique photothermal properties due to their strong plasmonic absorption in the near-infrared region of the electromagnetic spectrum. They have been explored widely as an alternative or complement to chemotherapy in cancer treatment. However, its use as an injectable medicine is greatly hindered by its stability in biological media. Therefore, studies were focused on improving the stability of AuNRs by introducing biocompatible surface functionalizations such as polyethylene glycol (PEG) coatings. However, these coatings can affect heat conduction and alter their photothermal behavior. Herein, we studied how functionalization of AuNRs with PEG chains of different molecular weights determined the temperature distribution of suspensions under near-infrared irradiation, cell uptake *in vitro*, and hyperthermia-induced cytotoxicity. Thermogravimetric analysis of the PEG-conjugated AuNRs exhibited slightly different PEG mass fractions of 12.0%, 12.7%, and 18.5% for PEG chains with molecular weights of 2, 5, and 10 kDa, implying distinct structures for the PEG brushes. When exposed to near-infrared radiation, we found greater temperatures and temperature gradients for longer PEG chains, while rapid aggregation was observed in unmodified (Raw) AuNRs. The effect of the PEG coating on heat transport was investigated using molecular dynamics simulations, which revealed the atomic scale structure of the PEG brushes and demonstrated lower thermal conductivity for PEG-coated AuNRs than for unmodified AuNRs. We also characterized the uptake of the AuNRs into mouse melanoma cells *in vitro* and determined their ability to kill these cells when subjected to near-infrared radiation. For all PEG-coated AuNRs, exposure to 10 s of near-infrared radiation significantly reduced cell viability relative to unirradiated controls, with this viability further decreasing with increasing AuNR doses, indicating potential phototherapeutic effects. The 5 kDa PEG coating appeared to yield the best performance, yielding significant phototoxicity at even the lowest dose considered (0.5 μg/mL), while also exhibiting high colloidal stability, which could help in rationale design consideration of AuNR for NIR induced photothermal therapy.

### 1. Introduction

Gold nanorods (AuNRs) have the potential to become a powerful tool in bio-imaging, cancer targeting, and cancer therapy, owing to the ease with which their surface chemistry can be modified and their ability to strongly absorb radiation in various regions of the electromagnetic spectrum.<sup>1–7</sup> The absorption of near infrared radiation (NIR) by AuNRs transforms light energy into thermal energy, which has been

extensively exploited in the hyperthermia-based therapy, so-called photothermal therapy.<sup>8,9</sup> In the NIR region, specifically at  $\lambda=808$  nm, light penetration is optimal due to minimal absorption from tissue chromophores and water. Therefore, surface plasmon resonance (SPR) induced heating is key to clinical therapy applications of AuNR involving superficial tumors, as well as those located deep within the bodily tissue (using optical fibers).<sup>10,11</sup>

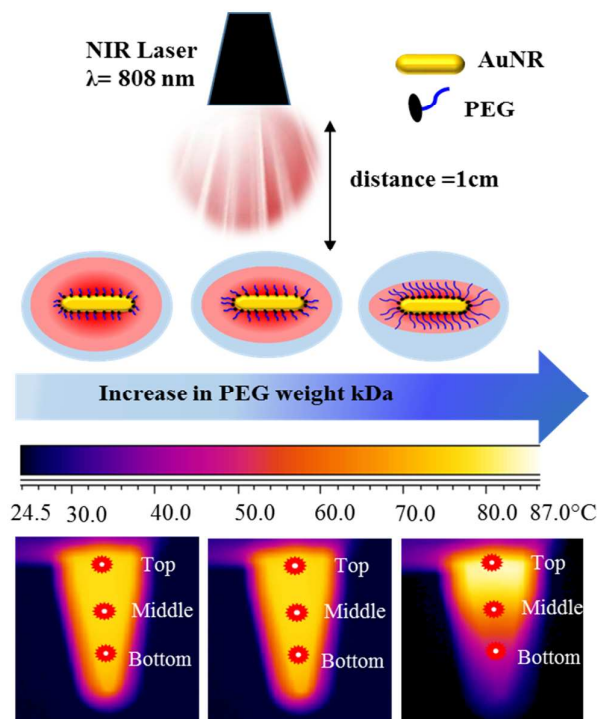
<sup>a</sup> Address here. Department of Chemistry, Kansas State University, Manhattan, KS 66506, Email: : [saryal@ksu.edu](mailto:saryal@ksu.edu)

<sup>b</sup> Nanotechnology Innovation Center of Kansas State (NICKS), Department of Anatomy and Physiology, Kansas State University, Manhattan, KS 66506

† Electronic Supplementary Information (ESI) available: [details of any supplementary information available should be included here]. See DOI: 10.1039/x0xx00000x

The large optical cross-sections of AuNR with tunable longitudinal surface plasmon resonance (LSPR) in the NIR makes them outstanding agents for photothermal therapy.<sup>6,9,12,13</sup> Given the large surface-area-to-volume ratio of AuNRs and the strong affinity of sulfur for gold surfaces, AuNRs can be conjugated with biomolecules like proteins, DNA, siRNA, and small-molecule drugs.<sup>14–17</sup> Therefore, AuNRs can be engineered to deliver therapeutics and to absorb NIR radiation for ablation of tumor cells, also known as cellular hyperthermia.<sup>18</sup> Selectivity is achieved by directional control or by using fiber optic positioning of the incoming radiation. For a tumor that is deeply situated inside the body, local cellular hyperthermia is achieved by the administration of AuNR and the local application of a pulsed or continuous wave laser source.<sup>19–24</sup> NIR laser pulses absorbed by AuNR excite free electrons in the plasmon band, creating a pulse of hot electrons. The hot electron pulse cools rapidly through electron–phonon interactions by colliding with the gold lattice, heating it to thousands of degrees (depending on laser power) within  $\sim 1$  ps.<sup>25</sup> Heat is then transferred from the nanorod to its surroundings through phonon–phonon interactions on a time scale of  $\sim 100$  ps, resulting in an increase in temperature of the surrounding medium by tens of degrees.<sup>26–28</sup> The enhanced heat in local tissue surrounding in turn causes cell death. This treatment modality, also known as plasmonic photothermal therapy, provides an attractive method for the treatment of solid tumors in a minimally invasive manner.<sup>24, 25</sup> El-Sayed et al. studied the feasibility of *in vivo* NIR photothermal therapy using AuNRs in mice bearing subcutaneous squamous cell carcinoma xenografts.<sup>29</sup> AuNRs were conjugated to thiol-terminated polyethylene glycol (PEG-SH) having a molecular mass of 5 kDa to increase biocompatibility, suppress immunogenic responses, and to decrease adsorption to the negatively charged luminal surface of blood vessels. A Greater than 96% decrease in average tumor growth was observed within 13 days.<sup>30–33</sup> Similarly, using AuNRs functionalized with Arg–Gly–Asp peptides (RGD), studies have demonstrated the inhibition of cancer cell migration by targeting integrins.<sup>34</sup>

Although the plasmonic properties of AuNRs have been highly exploited in biomedical research and applications, major concerns for achieving optimum photothermal effects are the colloidal stability of AuNRs in biological media and the blocking of heat transport from the surface of AuNRs to the surrounding medium by thick coatings. Therefore, suitable surface functionalization is necessary for stable, biocompatible and long-circulating nanoparticles.<sup>35–38</sup> Preferably, the surface passivating material should first have a strong affinity for the nanoparticle surface and also provide them with tunable chemical functionality, good colloidal stability, and biocompatibility.<sup>36</sup> PEG is common material for passivation of gold nanoparticles in physiological environments, yielding high colloidal stability, biocompatibility, long blood circulation time, and preferential accumulation in tumors.<sup>29,33,39,40</sup> However, heat transfer from AuNRs induced by NIR radiation is greatly affected by the physical properties of the surface-conjugated material. In particular, PEG passivation heavily influences



**Scheme 1.** Schematic showing the effect of surface passivation of gold nanorod with PEG molecules of various molecular masses (2, 5, 10 kDa) on plasmonic heating.

thermal conductivity at the gold–solvent interface, thereby altering photothermal effects at the macroscopic and microscopic levels.<sup>41,42</sup> A recent report from C. J. Murphy and coworkers demonstrated a decrease in the thermal conductivity of AuNR coated with the quaternary ammonium surfactant cetyltrimethylammonium bromide (CTAB), when the concentration of surfactant is above the critical micelle concentration.<sup>43</sup> The authors further extended their study by coating the AuNR surface layer-by-layer with polyelectrolytes and found an increase in thermal conductivity and heat capacity. It is clear that an optimizing the physical properties of the surface-conjugated ligand is important for the therapeutic outcomes. Herein, we investigated the jacketing effect of the PEG coating on photothermal cell ablation by varying the chain length of PEG conjugated to the surface of AuNR. AuNRs passivated with PEG of different molecular masses (2, 5, and 10 kDa) were studied in detail under NIR irradiation using a diode laser ( $\lambda = 808$  nm). Considering the higher NIR exposure for the surface cells versus that for deep tissue, we used a B16-F10 mouse melanoma cell line as an *in vitro* model to evaluate the therapeutic effectiveness of AuNRs.

## 2. Results and discussion

### Synthesis and surface functionalization of gold nanorods

NIR-responsive AuNRs were synthesized using seed-mediated growth methods.<sup>15</sup> The formation of AuNR was confirmed by observing its morphology using transmission electron microscopy and reading its longitudinal (LSPR) and transverse surface plasmon resonance (TSPR). The synthesized AuNRs were monodisperse with an aspect ratio of  $5.1 \pm 0.83$  and an average length of  $51.2 \pm 5.53$  nm with width of  $10.02 \pm 2.17$  nm (Figure 1 A). The LSPR and TSPR peaks of the as-synthesized AuNRs were found to be 840 nm and 510 nm, respectively. After surface functionalization with thiolated PEG of different molecular masses, LSPR peaks were found to be 850, 840, and 850 nm for AuNR-PEG-2, AuNR-PEG-5, and AuNR-PEG-10, respectively. Nonetheless, the TSPR peak

of the surface coatings. Thermogravimetric analysis was performed in an inert environment, and the mass of remaining metallic gold was recorded to permit calculation of the mass ratio between PEG and gold in the AuNRs. It is worth noting that metallic gold remains in the sample holder whereas the PEG completely decomposes as  $\text{CO}_2$  and other volatile compounds. Therefore, from the residual percentage of metallic gold, the mass fractions of PEG in AuNR-PEG-2, AuNR-PEG-5, and AuNR-PEG-10 were found to be 12.0%, 12.7% and 18.5%, respectively (Figure 1E). We further translated these percentages into the number of PEG molecule per AuNR and found 3478, 1307 and 1088 molecules of PEG, corresponding 2000, 5000, and 10000 Da PEG, respectively. Functionalization

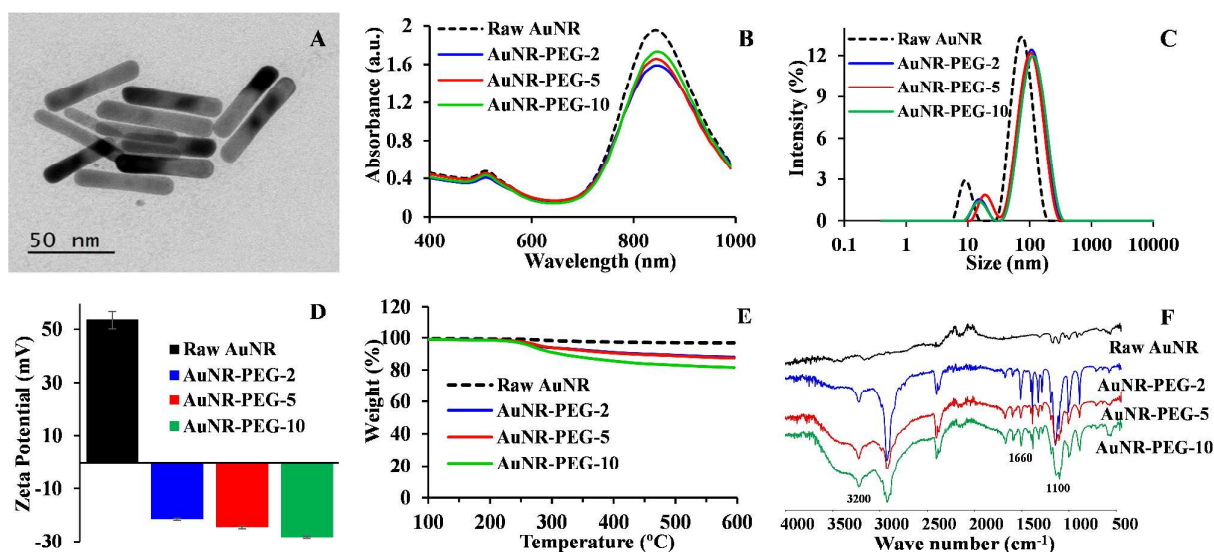


**Fig. 1** Physicochemical characterization of AuNRs before and after surface functionalization. (A) A representative transmission electron micrograph of as-synthesized AuNRs. (B) Surface plasmon resonance spectrum of NIR-responsive AuNRs before and after surface functionalization using PEG molecules of different molecular weights (viz., 2, 5, 10 kDa). (C) and (D) are the hydrodynamic size and zeta potential before and after PEG functionalization. (E) Thermogravimetric analysis for quantitative determination of PEG functionalization. (F) FTIR spectrum of the AuNRs verifying PEG conjugation on the surface of the AuNRs. The number 2, 5, and 10 in the nomenclature of each sample represents the corresponding molecular mass weight of the PEG molecules in kDa.

remained at 510 nm before and after PEGylation (Figure 1B).

#### Characterization of functionalized AuNRs

The surface coating efficiency of PEG onto the AuNRs surfaces was confirmed by measuring hydrodynamic diameter using DLS. The hydrodynamic size of the CTAB stabilized AuNR was found to be  $50.7 \pm 0.2$  nm in diameter, which when passivated with PEG reached  $79.36 \pm 0.14$ ,  $85.0 \pm 1.2$ , and  $80.0 \pm 0.13$  nm for AuNR-PEG-2, AuNR-PEG-5, and AuNR-PEG-10, respectively (Figure 1C). Additionally, the zeta potentials of Raw AuNR changed from positive  $+53.7 \pm 3.5$  mV to negative  $-21.5 \pm 0.4$ ,  $-24.5 \pm 0.5$ , and  $-28.3 \pm 0.4$  mV for AuNR-PEG-2, AuNR-PEG-5, and AuNR-PEG-10. These changes in zeta potential are indicative of successful surface functionalization (Figure 1D). The surface functionalized PEG shows higher colloidal stability at 4°C over the period (ESI, Figure S1).

With PEG modification supported by the DLS and zeta potential results, we moved to characterizing the density of

of the AuNRs by PEG was further corroborated by FTIR analysis (Figure 1F). The FTIR spectrum of Raw AuNR, AuNR-PEG-2, AuNR-PEG-5, and AuNR-PEG-10 strongly support the removal of CTAB (supporting information Figure S2) and the surface modification with the thiol PEGs. The peak at  $1100 \text{ cm}^{-1}$  is due to the etheral C-O stretching of PEG molecule while the peak at  $1600 \text{ cm}^{-1}$  is attributed to C-O stretching of the carboxyl group. The broad and very wide peak ranging from  $2400$  to  $3400 \text{ cm}^{-1}$  is due to the hydrogen bonded carboxyl group showing the surface functionalized with PEG moiety.

#### NIR photothermal efficiency

The photothermal efficiency of the Raw AuNR, AuNR-PEG-2, AuNR-PEG-5, and AuNR-PEG-10 were investigated under 808 nm NIR laser irradiation. All samples suspended in an aqueous solution were irradiated at the continuous wave constant diode laser power of  $21.2 \text{ W/cm}^2$  in a cell-free environment where the change in temperature versus time

was noted using a thermal imaging system (Forward Looking Infrared systems). As shown in Figure 2, a time-dependent increase in temperature was observed in all samples. For Raw AuNR, the temperature of the suspension reached up to  $56.3 \pm 2.9$  °C under NIR laser. In the case of AuNR-PEG-2, AuNR-PEG-5, and AuNR-PEG-10, the change in temperature was  $47.1 \pm 1.1$ ,  $57.1 \pm 2.7$  and  $69.2 \pm 2.7$  °C, respectively. However, during NIR exposure, a change in the color of the Raw AuNR suspension was observed, which was confirmed by recording the change in LSPR (Figure 3). This is presumably due to the fact that colloidal stability of AuNR is greatly affected by the local temperature, and high local temperature makes Raw AuNR unstable in the suspension (Scheme 1). To further elucidate the effect of NIR laser exposure on different PEG-modified AuNRs, we conducted a photothermal experiment where we measured the temperature at the top (point of NIR laser contact), middle, and bottom of the AuNR suspension. The distance between the top, middle and bottom positions were approximately 10 mm in depth. Figure 2 demonstrates that the temperature distribution was highly non-uniform in the case of AuNR-PEG-10, with a substantial change in temperature from  $69.2 \pm 2.7$  °C at the top (at the point of laser contact) to  $18.2 \pm 0.8$  °C at the bottom. The other AuNRs show more uniformity in temperature. These results suggest that higher molecular mass PEG may thermally insulate the AuNRs, supporting a higher temperature gradient.

Changes in the structural integrity and plasmonic properties of the AuNRs after NIR irradiation were investigated using transmission electron microscopy and UV-Vis spectrometry. As shown in Figure 3A, the Raw AuNR and AuNR-PEG-2 show significant changes in their LSPR peaks after NIR irradiation, which is possibly due to the temperature induced erosion of the AuNRs. For AuNR-PEG-5 and AuNR-PEG-10, the LSPR signals were quite stable even after NIR irradiation, which confirms the thermal stability of AuNRs after PEG grafting without negatively affecting their photothermal properties.

#### Thermal conductivity calculations

To better understand how the PEG coatings affected the heat conduction from the AuNR surfaces, we performed molecular dynamics simulations of PEG-conjugated gold surfaces and calculated the thermal conductivity through the PEG brushes. To make the simulations feasible and simplify the

**Table 1.** Thermal conductivity calculated in molecular dynamics simulations for PEG brushes of different PEG molecular masses and chain densities on a gold surface. The simulation systems were constructed for direct comparison to the experiments.

Simulation system	PEG molecular mass [kDa]	PEG chain density [ $\text{nm}^{-2}$ ]	Thermal cond. [ $\text{W}/(\text{K}\cdot\text{m})$ ]
A	–	0.0	$1.03 \pm 0.02$
B	2.0	1.98	$0.45 \pm 0.01$
C	5.0	0.86	$0.40 \pm 0.01$

analysis, we did not model complete AuNRs, but simply considered the structure of the PEG brush on flat slabs of gold. First, we compared the conductivity of a bare gold slab (Table 1, System A) to two models coated with PEG-SH molecules of different masses, mimicking the experiments. Systems B and C were conjugated with 2 and 5 kDa PEG molecules at densities of 1.98 and 0.86 molecules/ $\text{nm}^2$ , respectively, representing two types of nanorods used in the experiments (AuNR-PEG-2 and AuNR-PEG-5) (Figure 4). After relaxation, the 2 kDa PEG brushes appeared as shown in Figure 4A. In this case, the 2 kDa PEG chains completely crowd the surface, leaving little access to water. Indeed, the graph of the water density, Figure 4B, shows essentially no water within 4 nm of the gold surface, while the density of PEG near the gold surface is roughly the value of solid PEG. On the other hand, at the lower density of 5 kDa PEG molecules in System C, we observed less crowding of PEG near the surface, with significant amounts of water penetrating the brush. Because of the greater length of the PEG molecules, the brush in System C extended farther from the gold surface than of System B, reaching beyond 8 nm from the surface.

The thermal conductivity of the two PEG-containing systems and the bare gold system were calculated as described previously and detailed in the Methods section, by applying a constant heat current between a segment of the system near  $z = 0$  and a segment of the system near  $z = \pm 8.9$  nm.<sup>44</sup> Due to the use of periodic boundary conditions, the positions  $z = \pm 8.9$  nm are equivalent and in physical contact.

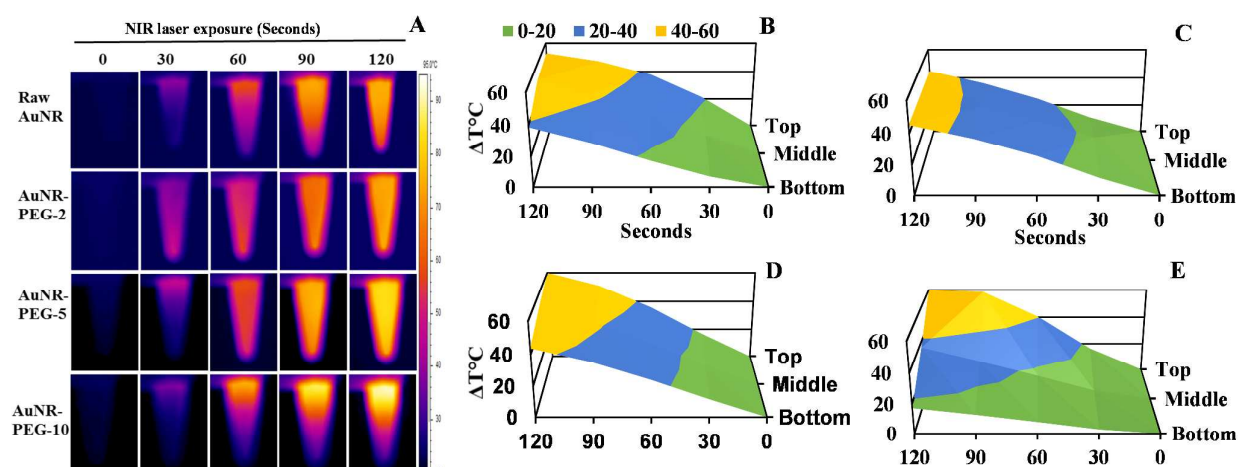


**Fig. 2** Photothermal properties of Raw and PEG-functionalized AuNRs. (A) Various AuNRs aqueous suspensions were irradiated with a near-infrared laser ( $\lambda=808$  nm,  $21.2$   $\text{W}/\text{cm}^2$ ) for 120 seconds and the evolution of temperature throughout the suspension was recorded using FLIR thermal camera system. (B), (C), (D), and (E) are the 3D temperature plots showing the average change in temperature as a function of time measured at the top, middle, and bottom of the AuNRs suspension of Raw AuNR, AuNR-PEG-2, AuNR-PEG-5, and AuNR-PEG-10, respectively.

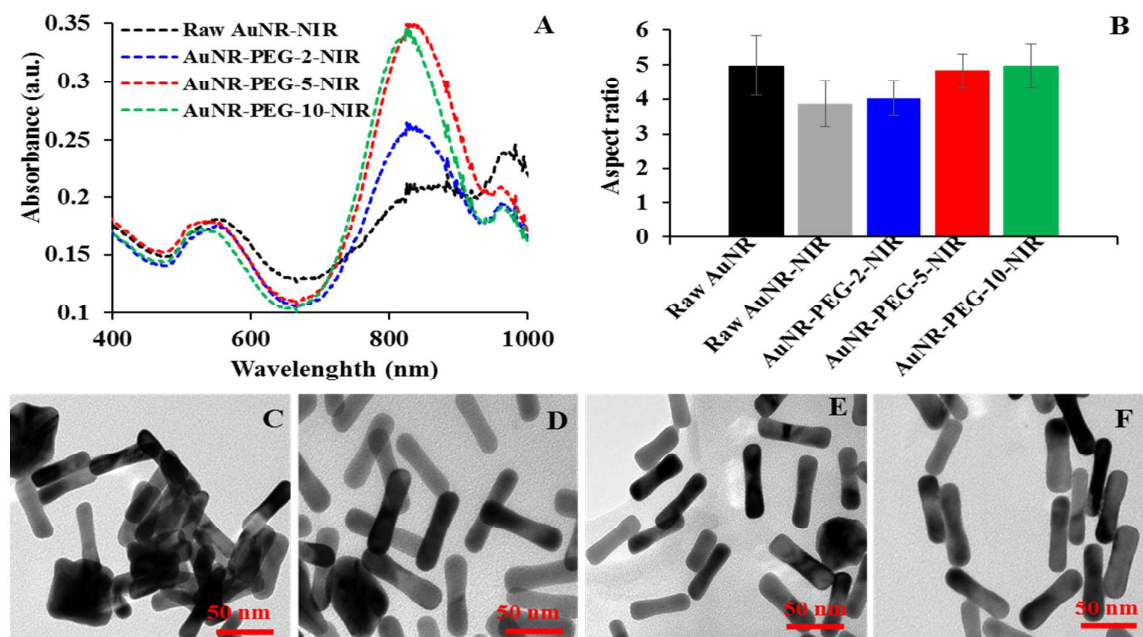


**Fig. 3** LSPR response and alteration in AuNR aspect ratio after NIR exposure of Raw and PEG passivated AuNRs. (A) UV-Vis spectrum showing changes in LSPR after NIR heating of both Raw and PEG passivated AuNRs. (B) The average aspect ratio of both Raw and PEG-functionalized AuNR after NIR heating. (C) Raw AuNR-NIR, (D) AuNR-PEG-2-NIR, (E) AuNR-PEG-5-NIR, and (F) AuNR-PEG-10-NIR are the representative transmission electron micrographs. Aspect ratio was calculated by measuring the length and width of 100 nanorods per sample. Scale bar 50nm.

The exact heat current depended slightly on the number of water molecules in each segment of the system, but in all cases, the average was in the range of 2.1–2.4  $\mu\text{W}$ . The average temperature distributions for the bare and PEG-coated slabs after reaching the steady-state are shown in Figure 4C. In the case of the bare slab, the calculation was simply a measurement of the thermal conductivity of bulk model water being a uniform medium; the temperature distribution appears linear. The thermal conductivity, as determined by the slope of this distribution is  $1.03 \pm 0.02 \text{ W}/(\text{m}\cdot\text{K})$ , shown in Table 1, is about 60% larger than that for real water at the same temperature<sup>45</sup> which is not surprising due to the fact that the flexible TIP3P water model used in the simulations has a higher self-diffusion coefficient than real water.<sup>46</sup> The temperature distribution of the PEG-coated gold surfaces (Figure 4C) is not uniform, due to the heterogeneity of these systems. The slope of the temperature profile is greatest for  $1.4 < |z| < 4.8 \text{ nm}$ , which also corresponds to the region of greatest PEG density (Figure 4B). The net temperature changes through the PEG brushes and water layer were 84 and 89  $^\circ\text{C}$ , more than twice that in the pure water system (39 $^\circ\text{C}$ ), leading to proportionately smaller conductivities. Although the temperature fell below 0  $^\circ\text{C}$  (Figure 4B) in some places, freezing was not and cannot be observed in these simulations.<sup>47</sup> The simulations support the notion that PEG conjugation acts to thermally insulate the gold nanorods from their environment, in agreement with the larger temperature gradients observed for the PEGylated nanorods in the experiment. Furthermore, as indicated in Table 1, the thermal

conductivity was smaller for the long 5 kDa PEG brush (System C) than for the shorter, higher density brush (System B), in agreement with the trend measured in the experiments.

#### Cellular Uptake Study

The cellular internalization efficiencies of Raw and PEG-modified AuNRs were investigated in mouse melanoma cell line B16-F10 using hyperspectral dark-field microscopy and ICP-MS. ICP-MS was used to evaluate the amount of gold taken up by cells after 6 and 24 hours of exposure. After 6 h of incubation, the cellular uptake efficiencies of Raw AuNR, AuNR-PEG-2, AuNR-PEG-5, and AuNR-PEG-10 were found to be 44, 23, 32 and 30%, respectively (Figure 5 A). For 24 h of incubation, the cellular uptake efficiency of Raw AuNR, AuNR-PEG-2, AuNR-PEG-5, and AuNR-PEG-10 were found to be 48, 28, 30 and 32%, respectively. The results indicate that the number of AuNRs taken up by B16-F10 cell is significantly greater for Raw AuNRs than for PEG-functionalized AuNRs. It is evident that PEGylation reduces the endocytosis of NPs and thus reduces its cellular internalization. No significant change was observed between different PEG-modified AuNRs even after 6 and 24 h incubation. It has previously been suggested that AuNRs are taken up via endocytosis and localized in endosomes within the cell.<sup>48</sup> Further qualitative analysis with hyperspectral dark-field imaging shows that Raw and PEG-modified AuNRs were taken up by the cells without significant loss of their structural integrity, as evidenced by their plasmonic signals inside the cell (Figure 5B, lower panel). The *in vitro* viability of cells containing Raw and PEG-coated AuNRs in the presence and the absence of the NIR laser was

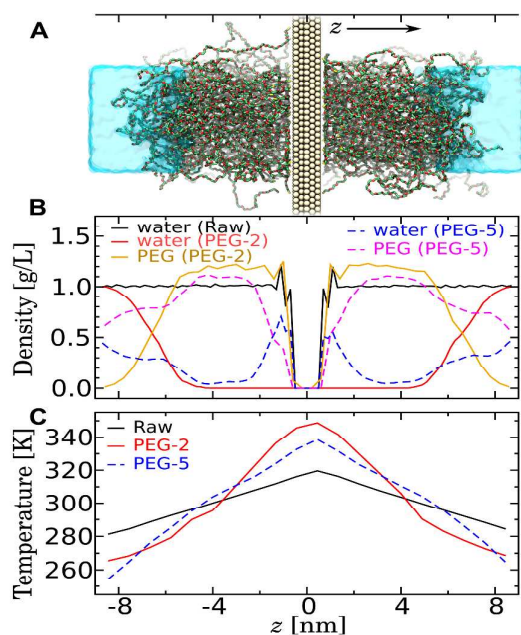


**Fig. 4** Molecular dynamics simulation of heat conduction through PEG brushes. (A) Snapshot of simulation System B for gold conjugated with 2 kDa PEG. The gold slab is shown as pale yellow spheres. The thiolated PEG molecules, illustrated in a bonds representation, are colored by atom type (C, green; O, red; S, yellow). For clarity, H atoms are not shown, and the explicit water molecules are illustrated as a cyan surface. Due to the use of periodic boundary conditions, the left and right ends of the system are in physical contact, and the PEG-coated gold surfaces have effectively infinite extent in the xy plane. (B) The mass density of water and PEG as a function of the z coordinate for Systems A (Raw), B (2 kDa PEG), and C (5 kDa PEG). The z scale is faithfully aligned with the image in panel A. (C) Steady-state temperature distribution in simulations where a constant heat current was induced in the system, permitting the thermal conductivity to be calculated. The larger temperature differences observed for the PEG-containing systems imply smaller thermal conductivities.

investigated in mouse melanoma B16-F10 cell lines after 24 h of AuNR treatment. For the photothermal therapy experiments, after 24 hours of treatment, the cell was irradiated with a NIR laser of wavelength 808 nm and power density of  $14.1 \text{ W/cm}^2$  for 10 seconds. Cell viability as a function of the AuNRs dose was observed (Figure 6A, upper panel).

#### NIR mediated phototoxicity study

For the Raw AuNRs, low cell viability was observed, even at a low dose of  $0.5 \mu\text{g/mL}$ , likely due to the cytotoxicity of residual CTAB surfactant. At the highest concentration tested ( $25 \mu\text{g/mL}$ ), the viability of cells with Raw AuNRs was found to be 20% in the presence of NIR radiation and 24% in its

comparison with Raw AuNRs, PEG-functionalized AuNRs (in the absence of NIR radiation) were found to be biocompatible with B16-F10 cells. At the highest concentration ( $25 \mu\text{g/mL}$ ) tested, the viability of AuNR-PEG-2 treated cells was found to be 60% in the absence of NIR radiation but was reduced to 28% after 10 s of NIR radiation. For AuNR-PEG-5, the cell viability was found to be 38% and 60% in the presence and absence of NIR radiation, respectively. For AuNR-PEG-10, the cell viability was found to be 30% and 60% in the presence and absence of NIR radiation (Figure 6A, upper panel). Therefore, for the PEG-modified AuNRs, we observed a significant reduction in cell viability caused by irradiation from the NIR laser, in contrast to the Raw AuNRs. Most importantly, among the different PEG

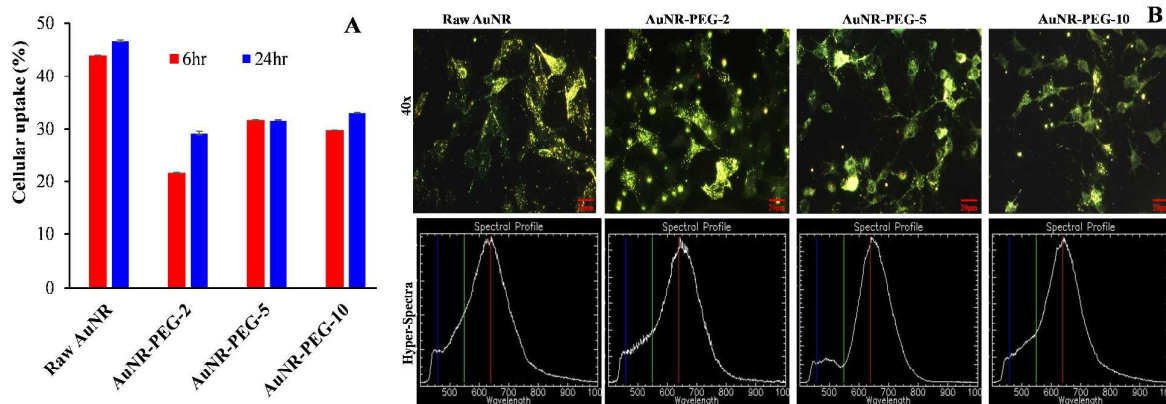


**Fig. 5** Cellular uptake efficiency of Raw and PEG-functionalized AuNRs with mouse melanoma cell line (B16-F10). (A) Quantitative cellular uptake of AuNR at incubation times of 6 and 24 h as measured by ICP-MS, and (B) Dark field hyperspectral microscopic images of B16-F10 cells treated with Raw and PEGylated AuNRs, and corresponding hyperspectral graph (lower panel) indicating the structural integrity of AuNRs inside the cells. Both LSPR and TSPR are visible, which is characteristic of AuNRs.

absences, a difference that was not statistically significant. In modifications, AuNR-PEG-5 exhibited significant phototoxicity

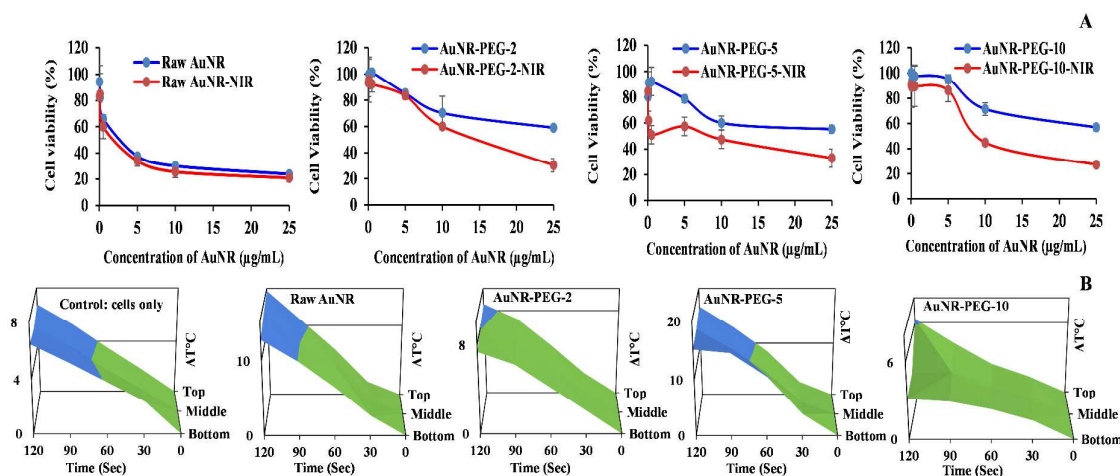


**Fig. 6** *In vitro* photothermal effect of Raw and PEG-functionalized AuNRs against B16-F10 Cells. (A), upper panel showing the phototoxicity of Raw AuNR and PEG-functionalized AuNRs before and after laser irradiation (irradiation time=10 s;  $\lambda=808\text{nm}$ ; and (B), the lower panel showing the change of temperature of Raw and PEG-functionalized AuNRs under laser irradiation in the cell suspension. The cells were previously incubated with AuNRs for 24 h and recovered as a cell suspension to study the NIR mediated thermal effect with same number of cells in all samples. The figures in the lower panel are the 3D temperature plots showing the average change in temperature at the top, middle, and bottom of the cell suspension. Cells without AuNRs treatment was used as control cell.

even at the lowest concentration tested ( $0.5\mu\text{g/mL}$ ), while higher concentrations were required to observe significant NIR- radiation-induced toxicity for AuNR- PEG- 2 and AuNR- PEG-10. The superior performance of AuNR-PEG-5 over the other AuNRs could be explained by Figure 3. During NIR treatment, the AuNR-PEG-2 nanorods appear to have been partially destroyed, as evident from the change in their aspect ratio shown in Figure 3B and TEM images C-E. As a result of partial thermal destruction, a relatively small temperature change of  $8 \pm 1^\circ\text{C}$  in the cell suspension was observed (Figure 6B, lower panel). Similarly, for AuNR-PEG-10, the thickness of the PEG brush hinders the heat transfer at the particle-polymer-water interface. Figure 6B, lower panel, provides great evidence of the pronounced effect in the case of AuNR-PEG-5 due to its thermal stability rendering efficient heat transfer to the surrounding thereby reaching cell suspension temperature to  $18 \pm 1.2^\circ\text{C}$  supporting results obtained from both experiment and molecular simulation.

### 3. Experimental Section

#### Chemicals and cell lines

Gold (III) chloride trihydrate ( $\text{HAuCl}_4 \cdot 3\text{H}_2\text{O}$ , 99.99%), cetyl tri- methyl ammonium bromide (CTAB, 99%), sodium borohydride (98%), L-ascorbic acid (99%), silver nitrate (99%), tris-hydrochloride (tris-HCl, 99%), and 3-(4, 5- methyl thiazol-2- yl)-2, 5-diphenyltetrazolium bromide (MTT) were purchased from Sigma-Aldrich (Milwaukee, WI, USA). Polyethylene glycol

carboxylic thiols (HOOC-PEG-SH) with average molecular masses of 2, 5, and 10 kilodaltons (kDa) were purchased from creative PEGWorks (North Carolina, USA). All other chemicals and reagents were of analytical grade and used as received from Fischer Scientific, USA. The mouse melanoma cell line B16–F10 was procured from ATCC and maintained in Dulbecco’s modified Eagle’s medium (DMEM) supplemented with 10% (v/v) fetal bovine serum (FBS) and penicillin/streptomycin ( $100\mu\text{g/mL}$ ) at  $37^\circ\text{C}$  in a 5%  $\text{CO}_2$  environment.

#### Synthesis of AuNR

NIR responsive AuNRs were synthesized using the seed-mediated growth method as described in earlier reports.<sup>13, 32</sup> In brief, the seed solution was prepared by adding  $250\mu\text{L}$  of  $\text{HAuCl}_4$  ( $0.01\text{M}$ ) into  $10\text{mL}$  of CTAB ( $0.1\text{M}$ ) under stirring. To this solution,  $600\mu\text{L}$  of freshly prepared ice cooled  $\text{NaBH}_4$  ( $0.01\text{M}$ ) was quickly injected and stirred for two minutes. For the growth solution,  $2\text{mL}$  of  $\text{HAuCl}_4$  ( $0.01\text{M}$ ) and  $0.4\text{mL}$  of  $\text{AgNO}_3$  ( $0.01\text{M}$ ) were added to  $40\text{mL}$  of CTAB ( $0.1\text{M}$ ) solution. The pH of the solution was adjusted to 1.0–2.0 using HCl ( $1.0\text{M}$ ) and subsequently  $0.32\text{mL}$  of ascorbic acid ( $0.1\text{M}$ ) was added to the solution under gentle mixing until the solution turned colorless. To form the AuNRs,  $0.096\text{mL}$  of the aged seed solution ( $2.5\text{h}$ ) was added to the growth solution under gentle mixing and incubated overnight at  $26^\circ\text{C}$ . The as-prepared AuNR solution capped with CTAB was stored at  $4^\circ\text{C}$  for further use.

#### Surface functionalization of AuNRs

Before surface modification, the excess CTAB present in the AuNR was removed by repeated centrifugation at 12,000 rpm for 10 mins. The AuNR pellet was re-dispersed in Milli-Q water and washed two times using the same conditions. After purification, the washed raw AuNR pellets were re-dispersed in 1 mL of tris-HCl (50 mM) (hereafter termed "Raw AuNR") and subsequently subjected to surface modification with the thiolated PEG (PEG-SH) of different molecular masses. For the process, 1 mL of PEG-SH (2, 5, or 10 kDa) with a concentration of 1 mg/mL dispersed in the 50 mM tris-HCl buffer (pH = 5) were used to functionalize the surface of purified AuNR (50 mg/mL in PBS) by rotating for 1 hour at room temperature. The resulting AuNRs are hereafter referred as "AuNR-PEG-2," "AuNR-PEG-5," and "AuNR-PEG-10." The number 2, 5, and 10 in the nomenclature of each sample represents the corresponding molecular mass of the surface-conjugated PEG chains in kDa. The excess of unreacted PEG was removed by centrifugation at 12000 rpm for 10 minutes, and the pellet was re-dispersed in PBS (1x) to make a final volume of 1 mL.

#### Characterization of functionalized AuNR

The surface plasmon resonance spectra of the as-prepared and surface modified AuNRs were analyzed using a UV-Vis spectrophotometer (BIOMATE-3S, Thermo Scientific) with 1.0 mm path length quartz cuvettes. The size and surface morphology were analyzed using a transmission electron microscope (FEI Technai G2 spirit Bio TWIN). The concentration of gold in all formulations were determined using inductively coupled plasma-mass spectroscopy (ICP-MS, Perkin Elmer, NEXION 350X) following standard protocol.<sup>37,49</sup> The hydrodynamic size, surface charge, and zeta potential analysis of the different AuNR formulations were carried out using dynamic light scattering (DLS, Zetasizer Nano ZSP, Malvern, Worcestershire, UK). Fourier transform infrared spectroscopic (FT-IR) analysis was performed to analyze surface chemistry of AuNRs using a Nicolet™ iS™ 50 FT-IR Spectrometer (Thermo Fisher).

#### NIR photothermal efficiency

The Photothermal effects of Raw AuNR and PEGylated AuNRs suspensions were determined in a cell-free environment. Briefly, a fixed concentration of Raw AuNR, AuNR-PEG-2, AuNR-PEG-5, and AuNR-PEG-10 (20 μg/mL) were irradiated using a continuous-wave NIR diode laser with a vacuum wavelength of 808 nm (0.6 mm spot focus size, power of 21.1 W/cm<sup>2</sup>) for 0, 30, 60, 90, and 120 s. The distance of the laser spot and AuNR suspension was maintained 1 cm for all samples (Scheme 1). During the irradiation, the temperature of AuNR suspensions in PBS (1x) was monitored by capturing images every 10 seconds using forward-looking Infrared (FLIR) thermal imaging system. For quantitative analysis, ThermoCAM™ Researcher Professional 2.8 SR1 software (FLIR system) was used to record temperature at three different locations of suspension (top, middle, and bottom) during NIR irradiation as demonstrated in Scheme 1.

#### Molecular Dynamics Simulations

The molecular models for performing the thermal conductivity calculations were constructed and equilibrated as described in the Supporting Information. Briefly, we created

three simulation systems mimicking the Raw AuNR, AuNR-PEG-2, AuNR-PEG-5 materials used in the experiments. The numbers of PEG chains per unit area of the gold surface were estimated from the geometry of the AuNRs and the mass fraction of PEG determined by electron microscopy and thermogravimetric analysis, respectively. Atomistic simulations of the AuNR-PEG-10 systems were deemed infeasible due to the size of the simulation system required for properly simulating PEG chains of that length. As illustrated in Figure 4A, each system contained a gold slab (simulated using the model of Wright et al. [ESI ref. 1]), water, and (except for the Raw system) thiol-terminated PEG chains<sup>50</sup> of the appropriate molecular masses (2 or 5 kDa). We did not attempt to model CTAB in the simulation systems since the thermogravimetric analysis showed that the mass fraction of CTAB on the Raw AuNR surfaces was relatively small (see Figure 1E). All simulation systems had approximately the same size (5.1 × 5.3 × 17.8 nm<sup>3</sup>) after equilibration at 300 K and atmospheric pressure. The thiolated PEG chains were relaxed in 100 ns of simulation using the program NAMD [ESI ref. 4] with the thiol groups in their reduced form, allowing the brush to self-assemble into realistic arrangement before the sulfur atoms were fixed to represent covalent attachment. Subsequently, the calculations of thermal conductivity were performed using the molecular simulation program LAMMPS.<sup>51</sup> The thermal conductivity through the system was calculated by the algorithm of Müller-Plathe.<sup>44</sup> A constant heat current (2.1–2.4 μW) was imposed between the center of the system (where the gold slab was located) and the extreme ends of the system by exchange of kinetic energies every 100 simulation steps. The resulting temperature distribution (considering 20 segments of the system along the z-axis) was measured after the system reached a steady state. Due to limitations of the Müller-Plathe algorithm's implementation in LAMMPS, covalent bonds to hydrogen and water molecules were made flexible during these simulations, requiring a 1 fs time step. The force field parameters used with NAMD were converted to LAMMPS format using a custom script (included in the ESI). The simulations were run at constant volume with the overall temperature maintained at 300 K by a Nosé-Hoover thermostat, which was previously shown not to affect the thermal conductivity calculations.<sup>44</sup> Each of the simulations was run more than 4 ns, with the convergence of the temperature distribution apparent after 0.5 ns. The thermal conductivity was calculated from the portion of the simulations for  $t > 1$  ns by  $\lambda = QL_z / (4A \Delta T \Delta t)$ , where  $Q$  is the total thermal energy transferred by the algorithm during the relevant simulation time  $\Delta t$ ,  $L_z$  is the z dimension of the simulation system ( $L_z/2$  is the distance between the centers of the hot and cold segments),  $A$  is the cross-sectional area of the system in the xy plane, and  $\Delta T$  is the average temperature difference between the hot and cold segments in the steady state.

#### Cellular uptake study

The cellular uptake and interaction of Raw AuNR, AuNR-PEG-2, AuNR-PEG-5, and AuNR-PEG-10 were studied with B16-F10 mouse melanoma cell line. ICP-MS and dark field

hyperspectral microscopy (Cytoviva Inc.) was used for quantitative and qualitative interaction studies. In short,  $10 \times 10^3$  B16-F10 cells were seeded in an 8-chambered glass slide and incubated for 24 hr. Monolayer adhered cells treated with the equivalent concentration of Raw AuNR, AuNR-PEG-2, AuNR-PEG-5, and AuNR-PEG-10 ( $5 \mu\text{g}/\text{mL}$ ) and incubated over the period (6 and 24 h). After incubation, an excess of AuNR was removed, and cells were washed with PBS and fixed with 4% paraformaldehyde. The cellular uptake was accessed by directly observing cells under a dark-field hyperspectral microscope, and the corresponding hyperspectral spectra of the Raw AuNR, AuNR-PEG-2, AuNR-PEG-5, and AuNR-PEG-10 were recorded, respectively.

#### Quantification of gold by ICP-MS

The concentration of gold (Au) in the cell was quantified by using ICP-MS following standard protocol.<sup>37,49</sup> Briefly, cells containing internalized AuNR were detached, washed and collected as a palette. Cell pallet were digested with  $1000 \mu\text{L}$  of aqua-regia (concentrated HCl and  $\text{HNO}_3$  3:1 by volume). The solutions were sonicated in hot water bath at  $60^\circ\text{C}$  for 45 min, followed by further dilution with  $4000 \mu\text{L}$  of 1%  $\text{HNO}_3$ . All analyses were performed on a PerkinElmer NexION<sup>®</sup> 350D ICP-MS using Syngistix<sup>™</sup> software (Shelton, CT, USA). To quantify the Au concentration, the calibration curve was developed based on the intensity and concentration of Au under the linear range. Under the optimized instrumental conditions and standard reaction mode, the limit of detection of Au was around 10 PPT, and the limit of quantification of Au was estimated at 50 ppt. The concentration of Au in the cell was determined after obtaining calibration curve of a various gold ion from commercial standards (1, 5, 10, 50 and 100 PPB).

#### Biocompatibility assay

The cytotoxicity assays of AuNRs before and after PEG passivation were carried out on mouse melanoma cell line B16-F10 using MTT assay. In brief,  $5 \times 10^3$  cells per well were seeded in 96-well plate and incubated for 24 hours. The seeded cells were washed twice with PBS to remove the debris before treatment. Then the medium was replaced with various concentrations of AuNRs (0.01, 0.1, 0.5, 5, 10, 25, and  $50 \mu\text{g}/\text{mL}$ ) suspended in DMEM. Control cell was maintained without treatment. The excess of particles was removed by washing with PBS. After 24 hours incubation, MTT was added to each well and further incubated for 4 h according to the manufacturer recommendation. The dark blue crystals generated by the live cells were dissolved in  $100 \mu\text{L}$  DMSO, and their absorbance was recorded at 570 nm using a microplate reader (BioTek, Synergy H1 hybrid reader).

#### NIR mediated phototoxicity assay in vitro

The photothermal effects of Raw AuNR and PEGylated AuNRs on B16-F10 cell line, in the presence and the absence of NIR laser exposure, were conducted using MTT assay. For this purpose,  $5 \times 10^3$  cells per well were seeded in a 96-well plate. When cells nearly reached to 85% confluency, Raw AuNR, AuNR-PEG-2, AuNR-PEG-5, and AuNR-PEG-10 (0.01, 0.1, 0.5, 5, 10, 25, and  $50 \mu\text{g}/\text{mL}$ ) were added and incubated for additional 24 hr. Cells without AuNRs and laser treatment was used as a control. At the end of incubation time, cells were

irradiated using a continuous-wave diode laser of wavelength 808 nm with a 1 mm spot focused size at a power of  $14.2\text{W}/\text{cm}^2$  for 10 seconds. After laser exposure, cells were incubated for additional 1 h at  $37^\circ\text{C}$  humidified with 5%  $\text{CO}_2$ . The cell viability was conducted by MTT assay.

## 4. Conclusions

In this study, we determined the influence of the PEG passivation on the AuNRs on their production of hyperthermia, with the aim to improve photothermal therapy of cancer. We compared unmodified, CTAB-stabilized AuNRs (Raw), with three PEG coatings of different PEG molecular masses (2, 5, and 10 kDa). AuNR-PEG-2 has a denser PEG coating than that of AuNR-PEG-5 and AuNR-PEG-10 as demonstrated by molecular simulation and supported by the quantitative thermogravimetric analysis. Therefore, there is little room for AuNR-PEG-2 on its surface for water diffusion as compared to the AuNR-PEG-10. However, due to intermediate chain length, relatively less dense coating, and higher thermal stability of 5 kDa induce more heat. Under a NIR laser, AuNR-PEG-5 shows a higher degree of structural stability and more uniform temperature distribution with enhanced NIR induced thermal toxicity against mouse melanoma cell line, B16-F10, as compared to AuNR-PEG-2 and AuNR-PEG-10. Therefore, this comprehensive fundamental study suggested an optimum polymer length of 5 kDa of PEG is advantageous for better surface passivation and colloidal stability of AuNR, which also maximizes the heat conduction from the nanorod–fluid interface to the surroundings to enhance its photothermal efficiency. Overall, this study illustrates the need for a proper selection of surface functionalizing agent in rationale design consideration of AuNR for biomedical applications.

## Conflicts of interest

There are no conflicts to declare.

## Acknowledgements

Authors acknowledged the support from the Johnson Cancer Research Center, Department of Chemistry, and the Nanotechnology Innovative Centre of Kansas State (NICKS), Kansas State University, Manhattan, Kansas.

## Notes and references

- 1 J. Stone, S. Jackson and D. Wright, *Wiley Interdiscip. Rev. Nanomed. Nanobiotechnol.*, 2011, **3**, 100–109.
- 2 D.-P. Yang and D.-X. Cui, *Chem. – Asian J.*, 2008, **3**, 2010–2022.
- 3 H. Huang, C. He, Y. Zeng, X. Xia, X. Yu, P. Yi and Z. Chen, *J. Colloid Interface Sci.*, 2008, **322**, 136–142.
- 4 C. Gui and D. Cui, *Cancer Biol. Med.*, 2012, **9**, 221.
- 5 E. Boisselier and D. Astruc, *Chem. Soc. Rev.*, 2009, **38**, 1759–1782.

- 6 C. J. Murphy, A. M. Gole, J. W. Stone, P. N. Sisco, A. M. Alkilany, E. C. Goldsmith and S. C. Baxter, *Acc. Chem. Res.*, 2008, **41**, 1721–1730.
- 7 S. Aryal, T. D. T. Nguyen, A. Pitchaimani, T. B. Shrestha, D. Biller and D. Troyer, *ACS Biomater. Sci. Eng.*, 2017, **3**, 36–41.
- 8 X. Huang, P. K. Jain, I. H. El-Sayed and M. A. El-Sayed, *Lasers Med. Sci.*, 2008, **23**, 217–228.
- 9 A. J. Gormley, N. Larson, A. Banisadr, R. Robinson, N. Frazier, A. Ray and H. Ghandehari, *J. Control. Release Off. J. Control. Release Soc.*, 2013, **166**, 130–138.
- 10 R. Weissleder, A clearer vision for *in vivo* imaging, [https://www.nature.com/articles/nbt0401\\_316](https://www.nature.com/articles/nbt0401_316), (accessed November 27, 2017).
- 11 A. M. Smith, M. C. Mancini and S. Nie, *Nat. Nanotechnol.*, 2009, **4**, 710–711.
- 12 H. Chen, Y. Guan, S. Wang, Y. Ji, M. Gong and L. Wang, *Langmuir ACS J. Surf. Colloids*, 2014, **30**, 13085–13091.
- 13 Y. Liu, M. Yang, J. Zhang, X. Zhi, C. Li, C. Zhang, F. Pan, K. Wang, Y. Yang, J. Martinez de la Fuentea and D. Cui, *ACS Nano*, 2016, **10**, 2375–2385.
- 14 S. Aryal, R. B.k.c., N. Dharmaraj, N. Bhattarai, C. H. Kim and H. Y. Kim, *Spectrochim. Acta. A. Mol. Biomol. Spectrosc.*, 2006, **63**, 160–163.
- 15 P. Arunkumar, B. Raju, R. Vasantharaja, S. Vijayaraghavan, B. Preetham Kumar, K. Jeganathan and K. Premkumar, *Nanomedicine Nanotechnol. Biol. Med.*, 2015, **11**, 1435–1444.
- 16 A. S. de Dios and M. E. Díaz-García, *Anal. Chim. Acta*, 2010, **666**, 1–22.
- 17 S. Aryal, J. J. Grailer, S. Pilla, D. A. Steeber and S. Gong, *J. Mater. Chem.*, 2009, **19**, 7879–7884.
- 18 X. Huang, P. K. Jain, I. H. El-Sayed and M. A. El-Sayed, *Nanomed.*, 2007, **2**, 681–693.
- 19 L. C. Kennedy, L. R. Bickford, N. A. Lewinski, A. J. Coughlin, Y. Hu, E. S. Day, J. L. West and R. A. Drezek, *Small Weinh. Bergstr. Ger.*, 2011, **7**, 169–183.
- 20 C. P. Nolsøe, S. Torp-Pedersen, F. Burcharth, T. Horn, S. Pedersen, N. E. Christensen, E. S. Olldag, P. H. Andersen, S. Karstrup and T. Lorentzen, *Radiology*, 1993, **187**, 333–337.
- 21 T. Vogl, M. Mack, R. Straub, S. Zangos, D. Woitaschek, K. Eichler and K. Engelmann, *Radiol.*, 2001, **41**, 49–55.
- 22 L. Tong, Y. Zhao, T. B. Huff, M. N. Hansen, A. Wei and J.-X. Cheng, *Adv. Mater.*, 2007, **19**, 3136–3141.
- 23 L. R. Hirsch, R. J. Stafford, J. A. Bankson, S. R. Sershen, B. Rivera, R. E. Price, J. D. Hazle, N. J. Halas and J. L. West, *Proc. Natl. Acad. Sci.*, 2003, **100**, 13549–13554.
- 24 D. P. O’Neal, L. R. Hirsch, N. J. Halas, J. D. Payne and J. L. West, *Cancer Lett.*, 2004, **209**, 171–176.
- 25 S. Link and M. A. El-Sayed, *Int. Rev. Phys. Chem.*, 2000, **19**, 409–453.
- 26 K. L. Kelly, E. Coronado, L. L. Zhao and G. C. Schatz, *J. Phys. Chem. B*, 2003, **107**, 668–677.
- 27 X. Liu, N. Huang, H. Li, H. Wang, Q. Jin and J. Ji, *ACS Appl. Mater. Interfaces*, 2014, **6**, 5657–5668.
- 28 D. A. Gobel, J. J. Yang and M. A. El-Sayed, *Chem. Rev.*, 1985, **85**, 529–554.
- 29 E. B. Dickerson, E. C. Dreaden, X. Huang, I. H. El-Sayed, H. Chu, S. Pushpanketh, J. F. McDonald and M. A. El-Sayed, *Cancer Lett.*, 2008, **269**, 57–66.
- 30 J. M. Harris and R. B. Chess, *Nat. Rev. Drug Discov.*, 2003, **2**, 214.
- 31 T. B. Huff, M. N. Hansen, Y. Zhao, J.-X. Cheng and A. Wei, *Langmuir*, 2007, **23**, 1596–1599.
- 32 H. Liao and J. H. Hafner, *Chem. Mater.*, 2005, **17**, 4636–4641.
- 33 T. Niidome, M. Yamagata, Y. Okamoto, Y. Akiyama, H. Takahashi, T. Kawano, Y. Katayama and Y. Niidome, *J. Control. Release Off. J. Control. Release Soc.*, 2006, **114**, 343–347.
- 34 X. Chen, Y. Hou, M. Tohme, R. Park, V. Khankaldyyan, I. Gonzales-Gomez, J. R. Bading, W. E. Laug and P. S. Conti, *J. Nucl. Med.*, 2004, **45**, 1776–1783.
- 35 G. von Maltzahn, J.-H. Park, A. Agrawal, N. K. Bandaru, S. K. Das, M. J. Sailor and S. N. Bhatia, *Cancer Res.*, 2009, **69**, 3892–3900.
- 36 A. Pitchaimani, T. D. T. Nguyen, H. Wang, S. H. Bossmann and S. Aryal, *RSC Adv.*, 2016, **6**, 36898–36905.
- 37 A. Pitchaimani, T. D. T. Nguyen, M. Koirala, Y. Zhang and S. Aryal, *Toxicol. In Vitro*, 2017, **43**, 29–39.
- 38 S. Aryal, C.-M. J. Hu and L. Zhang, *ACS Nano*, 2010, **4**, 251–258.
- 39 T. B. Huff, L. Tong, Y. Zhao, M. N. Hansen, J.-X. Cheng and A. Wei, *Nanomed.*, 2007, **2**, 125–132.
- 40 M. B. Koirala, T. D. T. Nguyen, A. Pitchaimani, S.-O. Choi and S. Aryal, *ACS Appl. Mater. Interfaces*, 2015, **7**, 27382–27390.
- 41 Z. Ge, D. G. Cahill and P. V. Braun, *J. Phys. Chem. B*, 2004, **108**, 18870–18875.
- 42 A. J. Schmidt, J. D. Alper, M. Chiesa, G. Chen, S. K. Das and K. Hamad-Schifferli, *J. Phys. Chem. C*, 2008, **112**, 13320–13323.
- 43 J. Huang, J. Park, W. Wang, C. J. Murphy and D. G. Cahill, *ACS Nano*, 2013, **7**, 589–597.
- 44 F. Müller-Plathe, *J. Chem. Phys.*, 1997, **106**, 6082–6085.
- 45 G. S. Kell, in *The Physics and Physical Chemistry of Water*, Springer, Boston, MA, 1972, pp. 363–412.
- 46 P. Mark and L. Nilsson, *J. Phys. Chem. A*, 2001, **105**, 9954–9960.
- 47 C. Vega, E. Sanz and J. L. F. Abascal, *J. Chem. Phys.*, 2005, **122**, 114507.
- 48 C. Grabinski, N. Schaeublin, A. Wijaya, H. D’Couto, S. H. Baxamusa, K. Hamad-Schifferli and S. M. Hussain, *ACS Nano*, 2011, **5**, 2870–2879.
- 49 A. Pitchaimani, T. D. T. Nguyen, L. Maurmann, J. Key, S. H. Bossmann and S. Aryal, *J. Biomed. Nanotechnol.*, 2017, **13**, 417–426.
- 50 H. Lee, R. M. Venable, A. D. MacKerell and R. W. Pastor, *Biophys. J.*, 2008, **95**, 1590–1599.
- 51 S. Plimpton, *J. Comput. Phys.*, 1995, **117**, 1–19.